Front. Mech. Eng. 2022, 17(3): 41
https://doi.org/10.1007/s11465-022-0697-z

RESEARCH ARTICLE

Piezoelectric inertial robot for operating in small pipelines based on stick-slip mechanism: modeling and experiment

Jichun XING (✉)[a], Chao NING[a], Yingxiang LIU (✉)[b], Ian HOWARD[c]

[a] *School of Mechanical Engineering, Yanshan University, Qinhuangdao 066004, China*
[b] *State Key Laboratory of Robotics and System, Harbin Institute of Technology, Harbin 150001, China*
[c] *School of Civil and Mechanical Engineering, Curtin University, Perth 6001, Australia*

✉ *Corresponding author. E-mails: xingjichun@ysu.edu.cn (Jichun XING); liuyingxiang868@hit.edu.cn (Yingxiang LIU)*

ABSTRACT Small pipes exist in industrial and biomedical fields, and require microrobots with high operational precision and large load capacity to inspect or perform functional tasks. A piezoelectric inertial pipeline robot using a "stick-slip" mechanism was proposed to address this requirement. In this study, the driving principle of the proposed robot was analyzed, and the strategy of the design scheme was presented. A dynamics model of the stick-slip system was established by combining the dynamics model of the driving foot system and the LuGre friction model, and the simulation analysis of the effect of system parameters on the operating trajectory was performed. An experimental system was established to examine the output characteristics of the proposed robot. Experimental results show that the proposed pipeline robot with inertial stick-slip mechanism has a great load capacity of carrying 4.6 times (70 g) its own mass and high positioning accuracy. The speed of the pipeline robot can reach up to 3.5 mm/s (3 mm/s) in the forward (backward) direction, with a minimum step distance of 4 μm. Its potential application for fine operation in the pipe is exhibited by a demonstration of contactless transport.

KEYWORDS pipeline robot, piezoelectric, inertial drive, stick-slip, large load capacity, dynamics model, small pipeline

1 Introduction

A wide range of small pipes, such as gas pipes, condensation tubes, test tubes, and human intestines, exists in the industrial and biomedical fields. These tubular structures have long lengths, relatively small inner diameters, and most of them have complex external geometric shapes [1–3]. Such pipelines create difficulty when performing inspection and maintenance operations. Thus, the demand for miniature pipeline robots that can achieve stable and accurate motion and carry actuators, such as probing instruments and work tools, is increasing [4,5].

Pipeline robots can be classified in accordance with the drive source as fluid driven, electric motor driven, hydraulic and pneumatic driven, electromagnetic driven, and functional material driven [6,7]. Depending on their characteristics, pipeline robots with different working principles play a crucial role in applications [8,9]. Fluid-driven pipeline robots, one of the first pipeline robots, are driven directly from the fluid without any additional power elements, and can only be driven effectively in large pipes with sufficient pressure [10,11]. The pipeline robot driven by electric motors is the most commonly used drive method and has the maximum drive speed and drive force in applications with larger pipe diameters [12–15]. However, it cannot enter the pipe or the driving speed and driving force are reduced when the pipe diameter is small due to the size of the motor and transmission device [16,17]. Hydraulic and pneumatic drives are mostly identical in terms of drive principle, and they can be applied to miniature-sized pipe robots. However, the essential hose for media transfer and control limits the use of pipe robots for long-distance inspection [18–22]. Electromagnetic field-driven pipeline robots are easy to miniaturize, especially the field-driven capsule robots using Helmholtz and Maxwell coils that can travel in the human intestine; however, their control system is more complicated, and the positioning accuracy is low [23–25]. The technology of using functional materials as the actuators of micro pipeline robots has

Received January 25, 2022; accepted April 19, 2022

received extensive attention in recent years, in which piezoelectric materials, shape memory alloys, and magnetostrictive materials present the characteristics of easy intelligence, integration, and miniaturization. Although the pipeline robots with memory alloy and magnetostrictive materials as actuators can realize locomotion in small pipes, their response speed and locomotion accuracy are relatively low and sensitive to ambient temperature due to the limitation of the characteristics of the actuators [26–29]. Piezoelectric materials have the advantages of small size, light mass, high displacement resolution, high energy density, and fast response [30,31]. The response speed, driving force, and control accuracy of miniature pipeline robots with piezoelectric materials are improved, which are better choices as the driving element [32–34].

Idogaki et al. [35] of Denso (Japan) first developed a pipeline robot using a piezoelectric stack that can perform inspection tasks in pipes with a diameter of 8 mm; this robot functions on the principle of "main body + mass block" inertial impact type. Tsuruta et al. [36] improved the previous structure by replacing the stacked piezoelectric actuator with a four-layered lead zirconate titanate bimorph actuator. Gong et al. [37,38] proposed two types of inertial impact pipeline robots with piezoelectric stack and piezoelectric bimorph as driving elements for vertical and horizontal locomotions, respectively. Liu et al. [1] and Sun [39] also developed an inertial impact type of pipeline robot with piezoelectric bimorph. Liu et al. [40] proposed different configurations to fabricate pipeline robots with piezoelectric materials. The abovementioned miniature pipe robots exhibit mainly inertial impact type motion of the "main body + mass block" pattern. Some researchers have explored alternative drive principles with piezoelectric materials. Yang et al. [41] proposed an approach of elliptical motion trajectory using ultrasonic vibrations of piezoelectric materials to excite the driving foot. Liu et al. [42] presented a pipeline robot in the form of bending and telescoping composite vibration using a piezoelectric stack. The new drive mechanism will enrich the advantages of piezoelectric material-driven pipeline robots and address the requirements of pipeline robots in different working conditions.

Most of the current inertia-driven pipeline robots use the "main body + mass block" inertia impact drive principle, which is good for miniaturization, large stroke, and high precision. However, most of the existing research focuses on the realization of inertia impact motion and ignores the problems of carrying actuators and operating in small pipes after miniaturization. The micro- and nano-scale fine manipulation in microelectromechanical systems and biomedical fields, such as manipulation of viruses or cells in test tubes and fine manipulation of biological tissues in outer space or in endoscopic tubes deep into the human body, has rapidly developed, especially in high-risk or inaccessible environments to humans. Therefore, small-sized pipeline robots that can perform precision operations with the capacity of large loads are urgently needed. For the development of a miniature pipeline robot with a large load and high position accuracy, a piezoelectric pipeline robot driven by the inertial stick-slip mechanism is proposed. This driving method is used for pipeline robots, which has not been reported before. The benefits of the proposed pipeline robot are its capability of bidirectional operation in small-sized pipes and carrying precision actuators of large mass, such as operating devices and endoscopes. The remaining parts of this paper are structured as follows. Section 2 illustrates the working principle and designed structure of the proposed pipeline robot. Section 3 demonstrates the modeling of the dynamic contact between the driving foot and pipe wall to analyze the drive process. Section 4 presents the fabricated prototype and discusses the experimental results and dynamic output characteristics. Section 5 provides the conclusions and perspectives of this work.

2 Working principle and structure

2.1 Working principle

An inertial actuator with the functional principle of the "stick-slip" mechanism usually employs a sawtooth wave signal (Fig. 1(a)) to supply the piezoelectric elements. In the stick phase, the piezoelectric actuator slowly expands along with the rising edge (slow positive ramp) of the drive signal, and then the slider moves with the driving object by a distance Δx due to the friction. In the slip phase, the piezoelectric actuator rapidly contracts with the falling edge (steep decay) of the drive signal, and the slider keeps the position due to the inertia, whereas the driving object moves to the original position. Thus, the slider moves a distance Δx with respect to the driving object (Fig. 1(b)). Inspired by this drive mechanism, the process is transformed into a drive method suitable for pipeline robots. In Fig. 1(c), the slider is transformed into a pipeline, and the driving object is transformed into a driving foot. The driving process of the proposed pipeline robot is explained in detail below.

1) Initial phase: When time $t = 0$, the drive signal is in the low-level stage, and the piezoelectric stack is not excited. Thus, the driving foot mechanism is not deformed, and the robot is in a rest state.

2) Stick phase: When the signal of the excitation voltage slowly rises during the time $0{-}t_1$ phase, the piezoelectric stack slowly elongates and pushes the driving feet to produce deformation. The friction force at the contact points between the driving feet and the inner

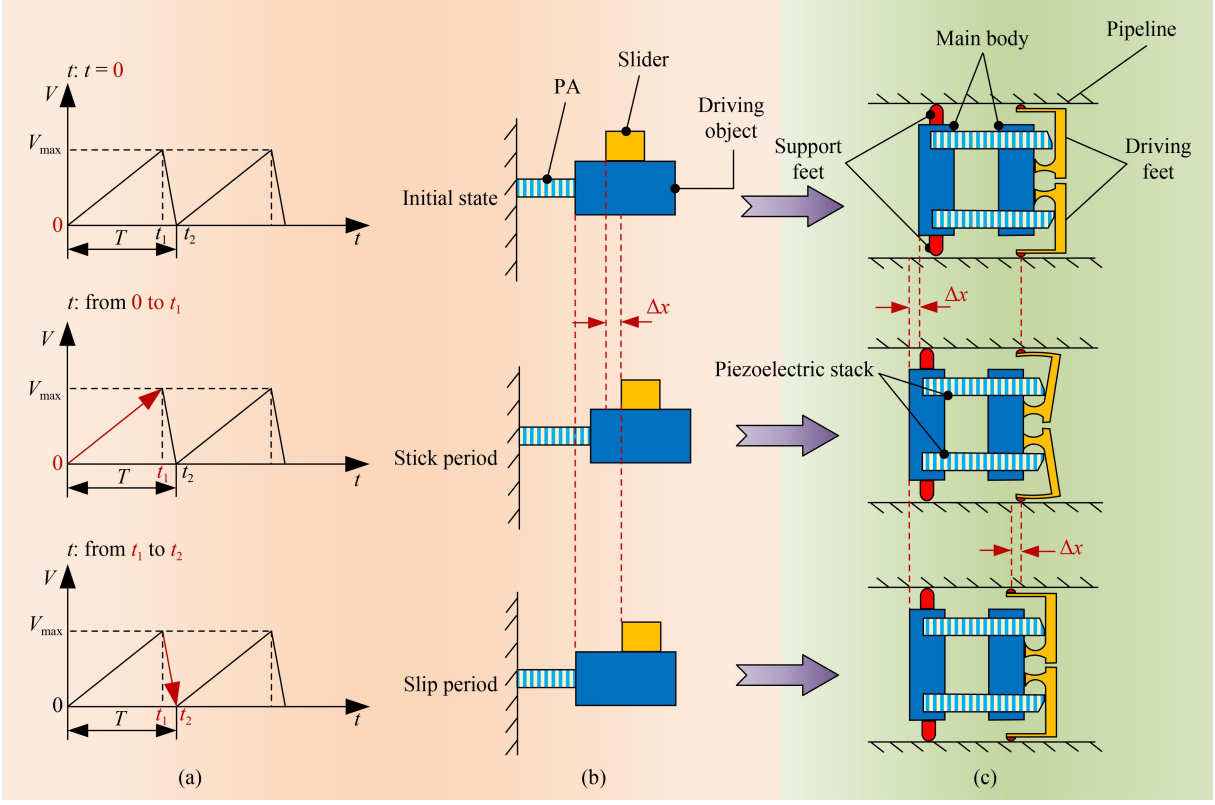

Fig. 1 Driving principle of the pipeline robot: (a) drive signal, (b) driving principle of "stick-slip," (c) driving principle of the proposed pipeline robot.

wall of the pipe is increased, and the contact points of the driving feet are relatively stationary with the pipe wall. The main body moves to the left by a distance Δx to comply with the deformation of the driving foot. Here, the frictional force between the Δx support feet and the pipe wall is set to be smaller than the thrust of the main body.

3) Slip phase: When the drive signal is in the phase of time t_1–t_2, the voltage of the drive signal declines rapidly from the maximum value to zero, and the piezoelectric stack contracts rapidly. The driving feet restore deformation due to the flexure hinge recovery force. At this time, the friction force between the contact points of the driving feet and the pipe wall is reduced. The position of the body relative to the pipe remains unchanged, and the relative slip between the driving feet and the pipe wall occurs because of the inertial force of the main body. Therefore, the pipeline robot as a whole will be displaced to the left by Δx. However, in practice, the process still has a backward phenomenon, so the actual displacement will be slightly smaller than Δx.

The above described process can be repeated to achieve the continuous stepping motion of the proposed pipeline robot. The step length, speed, and motion direction of the robot can be controlled by adjusting the drive voltage amplitude, frequency, and duty cycle of the sawtooth wave.

2.2 Structure design

The devised pipeline robot is presented in Fig. 2 in accordance with the analysis of the operating principle. The main components of the proposed pipeline robot include two piezoelectric stacks, a main body, four support feet, and two driving feet. The main body is composed of two blocks, which use a hollow structure to minimize the mass of the main body. Four support feet are evenly distributed around the body and are bolted to the body. The bending structure of the support foot can provide the pre-pressure to the pipe wall and adapt to the various diameters of the pipeline by adjusting the screws. Two piezoelectric stacks are symmetrically embedded into the body with a preload provided by screws. Two flexure hinges with restoring force are mounted on one block of the main body, which amplifies the output displacement of the piezoelectric stack and supports the rotation of the driving feet. The driving foot mounted on the flexure hinge is an L-shaped plate spring with a half-sphere contact point that is set at the cantilever end to interact with the pipe wall. For the other block of the main body, a mounting hole is devised to assemble the camera module, injectors, and noncontact gripper. The proposed pipeline robot limited by the size of selected piezoelectric stacks (20 mm × 5 mm × 5 mm) has the

capacity to adapt the range of the pipeline diameter of 25–35 mm. Therefore, it can further be miniaturized.

3 Modeling and analysis of the driving process

3.1 Modeling of the driving process

A dynamic model considering the dynamic frictions needs to be established to describe the driving process and investigate the dynamic behavior theoretically. The physical model must be simplified to a dynamics model. Half of the structure of the pipeline robot is taken as a research object that includes a piezoelectric stack, a flexure hinge, a driving foot, and the pipe wall due to the symmetrical structure of the proposed pipeline robot. In actual operation, the robot is in motion, and the pipe is stationary. For ease of analysis, the robot is assumed to be motionless and the pipe moves relative to the robot to build the dynamic model, as shown in Fig. 3.

In Fig. 3, the equivalent mass of the piezoelectric stack is denoted by m_1, the equivalent mass of the flexure hinge is denoted by m_2, the equivalent mass of the driving foot is denoted by m_3. Here, the pipeline is equivalent to a beam with the equivalent mass denoted by m_4. Considering the transition of the motion state of the robot and the pipe and the measurement of inertial forces in the equilibrium equation, the magnitude of the mass m_4 is equivalent to the overall mass of the robot. x_1 is the output displacement of the piezoelectric stack, that is, the input displacement of the system. x_2, y_3, and x_4 denote the displacements of mass blocks m_2, m_3, and m_4, respectively. k_1, k_2, and k_3 denote the equivalent stiffness

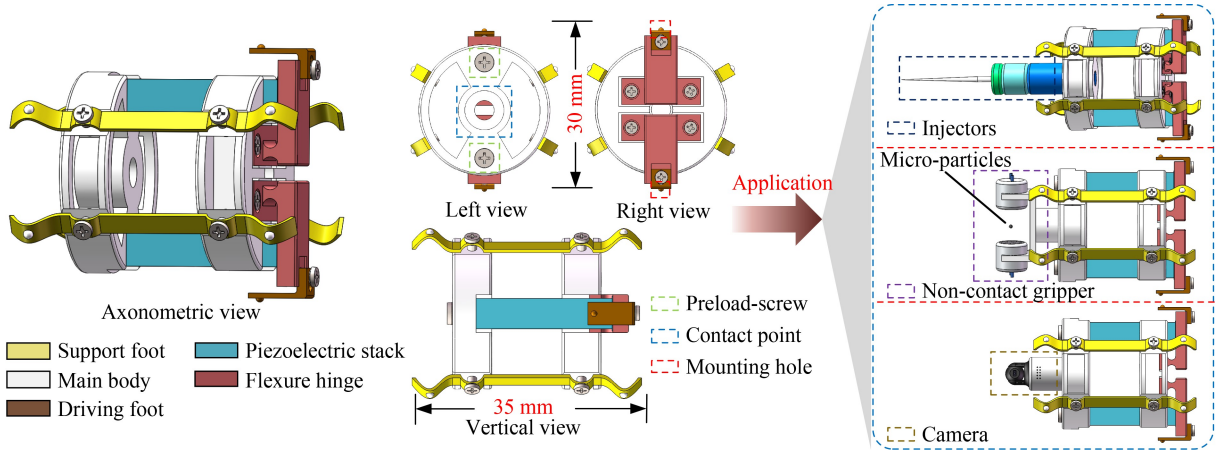

Fig. 2 Configuration of the devised pipeline robot and portable devices for the application.

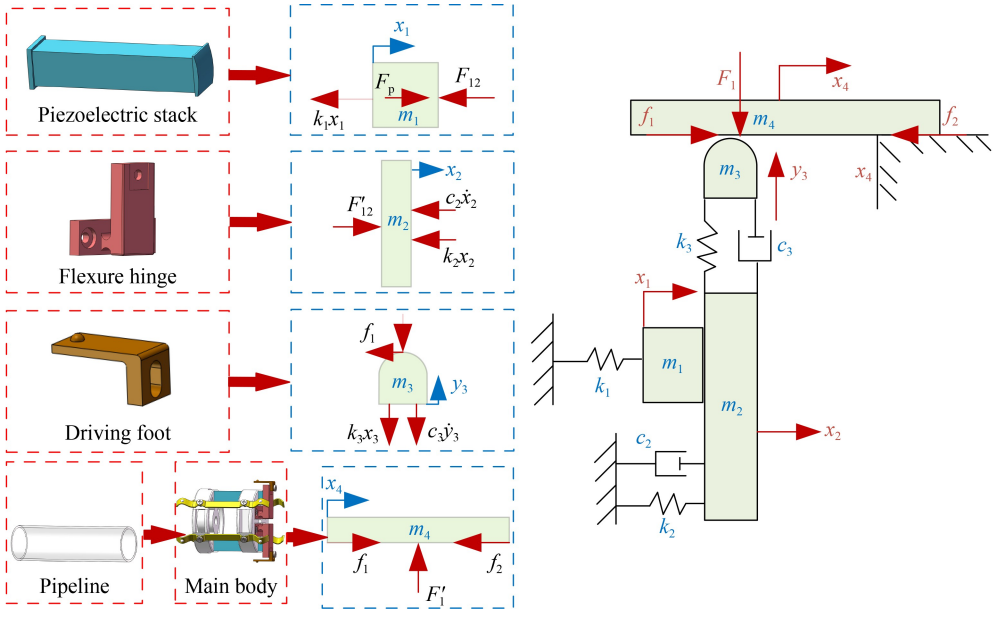

Fig. 3 Dynamic model of the proposed pipeline robot.

of the piezoelectric stack, flexure hinge, and plate spring, respectively, and c_2 and c_3 denote the equivalent damping of the flexure hinge and plate spring, respectively. F_{12} and F'_{12} are the acting force and reacting force between the piezoelectric stack and the flexure hinge. F_1 and F'_1 are the acting force and reacting force between the driving foot and the pipe wall.

In accordance with Newton's Second Law, the equations describing the dynamics behavior can be presented as

$$\begin{cases} (m_2+m_3)\ddot{x}_2 = F_\mathrm{p} - k_2 x_2 - c_2\dot{x}_2 - f_1, \\ m_3\ddot{y}_3 = F_1 - k_3 y_3 - c_3\dot{y}_3, \\ m_4\ddot{x}_4 = f_1 - f_2, \end{cases} \tag{1}$$

where F_p is the output force of the piezoelectric stack at an output displacement of x_1, F_1 is the pressure of the driving foot on the pipe wall, f_1 is the friction between the driving foot and the pipe wall, and f_2 is the friction between the support foot and the pipe wall. From Ref. [43], the output force F_p of the piezoelectric stack can be written as

$$F_\mathrm{p} = k_1 n d_{33} U - k_1 x_1, \tag{2}$$

where n is the number of the piezoelectric sheets in the piezoelectric stack, U is the voltage of the drive signal, and d_{33} is the piezoelectric coefficient. The stiffness k_1 of the piezoelectric stack can be calculated as $k_1 = A/(s_{33}L_\mathrm{p})$, where A is the cross sectional area of the piezoelectric stack, L_p is the length of the piezoelectric stack, and s_{33} is the elastic compliance coefficient of the piezoelectric stack.

In Eq. (1), the pressure F_1 of the driving foot is varied with the position of the contact point. Thus, the friction f_1 determined by F_1 is a varying force in the operation process. The cause of the change in force F_1 can be illustrated in Fig. 4. The generation of displacement x_2 is determined by the rotation angle θ_1 of the flexure hinge. If the driving foot has no constraint, then the contact point will have a displacement y_3 at a rotation angle θ_2. However, the pipe wall restricts the position of the driving foot and creates a deformation of the driving plate spring. The value of the pressure F_1 is determined by the unconstrained displacement y_3 of the contact point due to the angle of rotation θ_1. In Fig. 4, l is the length from the rotation center to the top of the flexure hinge displacement amplification structure, l_1 is the distance from the center of rotation of the hinge to the point of action with the piezoelectric stack, l_2 is the vertical distance from the top of the flexure hinge to the center of rotation under rotation θ_1, l_3 is the vertical distance between the top of the hinge and the initial position after rotation θ_1, and l_4 is the length of the driving foot. Given that the elongation of the piezoelectric stack is in the order of microns, the rotation angle θ_1 of the flexure hinge will be extremely small and can be approximated as

$$\theta_1 = \frac{x_1}{l_1}. \tag{3}$$

From Fig. 4(b), the relationship between y_3 and x_1 can be derived from the geometric features as

$$y_3(t) = l_4 \sin\frac{x_1}{l_1} - l_3. \tag{4}$$

The relationship between the output displacement and the pressure F_1 can be obtained by substituting Eq. (4) into Eq. (1). The dynamic model of the friction f_1 is established by employing F_1.

The dynamic friction model is introduced to consider the hysteresis phenomenon, variable static friction, and the Stribeck effect, and to accurately describe the nonlinear stick-slip driving principle. In accordance with the LuGre model, the frictional contact between the contact point of the driving foot and the pipe wall is simulated as the contact of two surfaces with elastic

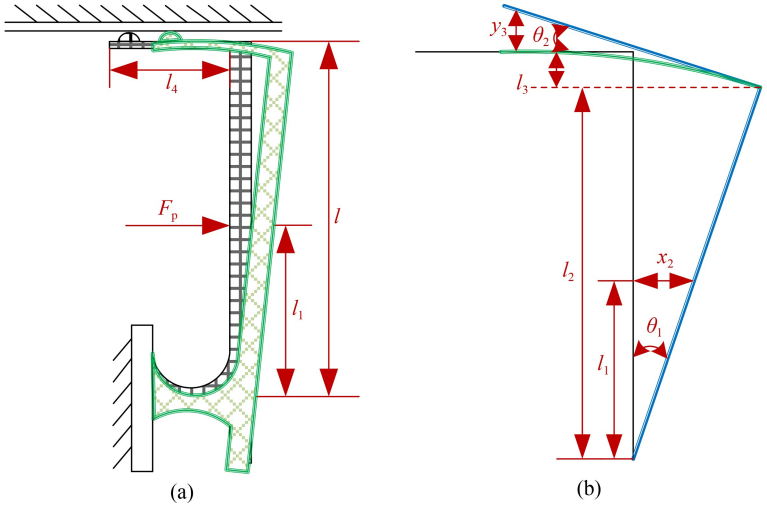

Fig. 4 Analysis of the force and geometric relationship of the driving foot: (a) deformation of the driving foot and (b) geometric relationship of the driving foot.

bristles. When a tangential force is applied, the bristles deform similar to a leaf spring, generating a frictional force. The bending displacement of the bristles is random due to the irregularity of the friction surface, and the LuGre model can be expressed as [44]

$$\frac{\mathrm{d}z}{\mathrm{d}t} = v - \frac{|v|}{g(v)}z, \tag{5}$$

where v is the relative velocity of two friction surfaces, that is, $v = \dot{x}_4 - \dot{x}_2$, z is the average deformation of bristles, and $g(v)$ is a function describing the Stribeck effect. In Ref. [45], the function $g(v)$ is derived as

$$g(v) = \frac{F_\mathrm{C} + (F_\mathrm{S} - F_\mathrm{C})\exp\left(-\left(\frac{v}{v_\mathrm{s}}\right)^2\right)}{\sigma_0}, \tag{6}$$

where F_C is the Coulomb friction force, F_S is the static friction force, v_s is the velocity when the Stribeck effect occurs, and σ_0 is the stiffness of the bristles. The Coulomb friction force can be calculated as $F_\mathrm{C} = \mu F_1$, where μ is the friction coefficient between the driving foot and the pipe. The friction force generated by the deflection of bristles can be expressed as

$$f_1 = \sigma_0 z + \sigma_1 \frac{\mathrm{d}z}{\mathrm{d}t} + \sigma_2 v, \tag{7}$$

where σ_1 is the damping coefficient of the bristle, and σ_2 is the viscous damping coefficient. If the bristles are in the steady-state motion, then $\mathrm{d}z/\mathrm{d}t = 0$. Thus, the relation between velocity and friction force for the steady-state motion in accordance with Eqs. (5)−(7) is expressed as

$$f_1 = F_\mathrm{C}\mathrm{sgn}(v) + (F_\mathrm{S} - F_\mathrm{C})\exp\left(-\left(\frac{v}{v_\mathrm{s}}\right)^2\right)\mathrm{sgn}(v) + \sigma_2 v. \tag{8}$$

In accordance with the characteristic of the moving process, the "slip-stick" motion of the pipeline robot can be divided into four phases. The movement state of each phase of the system is analyzed and discussed by using the LuGre model of the dynamic friction force. In our hypothesis of the system model, the runner is the pipeline. Thus, the dynamic equations in each phase are presented separately with it as the research object.

(1) Initial "stick" phase: The state between the driving foot and pipe wall can be considered the preload phase. At this moment, the friction between the contact point of the driving foot and the pipe belongs to the category of static friction. However, as described by the LuGre model, the small deformation z of two contact surfaces can be regarded as the occurrence of relative displacement x_4, that is, $z = x_4$. Substituting Eq. (7) into the equation that describes the motion of runner m_4 in Eq. (1) and assuming right is the positive direction, the dynamics equation describing this phase can be obtained as

$$-m_4\frac{\mathrm{d}^2x_4}{\mathrm{d}t^2} = \sigma_0 z + \sigma_1\frac{\mathrm{d}z}{\mathrm{d}t} + \sigma_2 v - f_2. \tag{9}$$

With $z = x_4$ and $v = \mathrm{d}x_4/\mathrm{d}t$, Eq. (9) can be rearranged as

$$m_4\frac{\mathrm{d}^2x_4}{\mathrm{d}t^2} + (\sigma_1 + \sigma_2)\frac{\mathrm{d}x_4}{\mathrm{d}t} + \sigma_0 x_4 - f_2 = 0. \tag{10}$$

(2) "Stick" phase: The runner is driven by the contact point of the driving foot and moves together. From the macroscopic point of view, no relative displacement occurs between the runner and the contact point of the driving foot. From the microscopic point of view, the two still maintain the relative displacement z in the initial "stick" phase, and the friction force is still static at this time based on the LuGre model. Since the displacement z is not increasing, the friction force of the LuGre model can be written as $f_1 = \sigma_0 z$. Thus, the equations that can describe the dynamic behavior of the runner in this phase are written as

$$m_4\frac{\mathrm{d}^2x}{\mathrm{d}t^2} - \sigma_0 z + f_2 = 0. \tag{11}$$

(3) "Slip" phase before velocity $\dot{x}_4 = 0$: In this phase, the voltage of the drive signal has a steep decay, and the driving foot restores to its original shape with the piezoelectric stack. A substantial relative sliding motion occurs between the contact point of the driving foot and the runner due to the inertia. The runner starts to decelerate under the action of friction forces f_1 and f_2 until the velocity is zero. This phase is named the preslip-zero phase. If the right side is the positive direction, then the dynamics equation describing this phase can be obtained as

$$m_4\frac{\mathrm{d}^2x_4}{\mathrm{d}t^2} = -\left(\sigma_0 z + \sigma_1\frac{\mathrm{d}z}{\mathrm{d}t} + \sigma_2 v\right) - f_2. \tag{12}$$

In this phase, the average tangential bending displacement of the bristles in the LuGre model can be regarded as reaching the steady state, that is, $\mathrm{d}z/\mathrm{d}t = 0$. Thus, the dynamic equation of the preslip-zero phase can be rearranged as

$$m_4\frac{\mathrm{d}^2x_4}{\mathrm{d}t^2} + \sigma_2 v + \sigma_0 z + f_2 = 0. \tag{13}$$

(4) "Slip" phase after velocity $\dot{x}_4 = 0$: During the phase of restoring the deformation of the driving foot, the runner may follow the driving foot to move back a certain distance due to the existence of sliding friction between the driving foot and the runner after the velocity decreases to 0. The retreating distance is called the backlash. The runner is a reverse acceleration process before the arrival of the next periodic signal. The dynamic equation is rewritten as

$$m_4\frac{\mathrm{d}^2x_4}{\mathrm{d}t^2} + \sigma_2 v + \sigma_0 z - f_2 = 0. \tag{14}$$

3.2 Simulation analysis

In the "slip" phase, the runner is in a process of deceleration and then reverse acceleration. The driving

foot overcomes the friction before the next stick motion arrives to complete the deformation recovery, where it is ready to start the initial "stick" phase again. The motion process of the pipeline robot is simulated by using the equations of motion established above to investigate the motion state of the robot in one cycle and the effect of the system parameters on the drive performance. The system parameters of the pipeline robot can be obtained by testing and referring to Refs. [44,45]. The detailed values of these parameters are listed in Tables 1–3.

The system parameters in Tables 1–3 are substituted into the dynamic equations of the four phases. The motion trajectory of the runner in one cycle of the drive signal is presented in Fig. 5(a). Given that the motion states of the pipe and the robot are transformed relatively to establish the dynamics equations, the motion state of the runner in Fig. 5(a) reflects the motion state of the robot. The key parameters the equivalent mass m_4 of the pipe, the stiffness k_2 of the flexure hinge, and the stiffness of the driving foot k_3 are selected to investigate the effect on the motion state of the runner. The motion trajectory curves of the runner with different variables are presented in Figs. 5(b)–5(d).

Table 1 Parameters of the employed piezoelectric stack

Symbol	Quantity	Value
d_{33}	Piezoelectric coefficient	635 pm/V
S_{33}	Elastic compliance constant of the piezoelectric stack	18.1×10^{-12} m^{-2}/N
L_p	Length of the piezoelectric stack	20 mm
A	Cross section area of the piezoelectric stack	25 mm^2
n	Number of the piezoelectric sheets	181
V_{max}	Peak voltage of the drive signal	120 V
x_{1max}	Maximum output displacement of the piezoelectric stack	15 μm

Table 2 Parameters of the LuGre model

Symbol	Quantity	Value
F_S	Maximum static friction	0.025 N
μ	Friction coefficient	0.78
σ_0	Bristle stiffness	10^5 N/m
σ_1	Bristle damping	$10^{5/2}$ N·s/m
σ_2	Viscous damping coefficient	0.4 N·s/m
v_s	Stribeck velocity	0.001 m/s
f_2	Friction between support foot and pipe wall	0.03 N

Table 3 Parameters for the structure properties of the robot

Symbol	Quantity	Value
k_2	Stiffness of the flexure hinge	3.9×10^6 N/m
c_2	Damping of the flexure hinge	0.002 N·s/m
k_3	Stiffness of the driving foot	1.8×10^5 N/m
c_3	Damping of the driving foot	0.008 N·s/m
m_2	Equivalent mass of the flexure hinge	0.66 g
m_3	Equivalent mass of the driving foot	0.15 g
m_4	Equivalent mass of the pipe	13.38 g

In Fig. 5(a), area a is the initial "stick" phase of the system, where the runner enters area b of the stick phase in a relatively short period of time, that is, the preload between the driving foot and the pipe wall is completed in a relatively short period of time. In area b, the contact point of the driving foot sticks to the pipe wall, and the deformation of the driving foot increases with the increase in the drive signal voltage. Therefore, a large relative displacement of the main body to the pipe wall occurs at this phase. When the drive voltage reaches its peak and the drive signal is about to turn to the falling edge, the pipeline robot still moves forward due to the inertial force. From the area c, this state is maintained for an extremely short time, and the relative distance produced is extremely small. When the drive signal is at the falling edge, the driving foot quickly recovers its deformation, and the driving foot contact point is in the "slip" phase with the pipe wall due to inertia. However, the runner may follow the driving foot to move backward a certain distance owing to the sliding friction between the driving foot and the runner, that is, the backlash, as shown in area d. In one cycle, the actual step distance of the pipeline robot is Δx.

From Fig. 5(b), the output displacement decreases with the increase in the runner mass (i.e., the main body mass) during an operating cycle. Specifically, larger runner masses (i.e., body masses) produce smaller relative displacements for the proposed robot during the "stick" phase and smaller backlash during the "slip" phase. This condition is because larger masses of the main body have larger inertial forces. Therefore, if a higher step resolution and smaller backlash are required, then the robot body mass can be increased appropriately for the design. Similarly, a larger flexure hinge stiffness corresponds to a smaller displacement output. However, it has a limited effect on the reduction of the backlash, as shown in Fig. 5(c). Figure 5(d) shows that the increase in the stiffness of the drive plate spring increases the relative displacement generated in the stick phase and the amount of backlash in the slip phase, but the overall output displacement is slightly larger. Therefore, the stiffness of the drive plate spring can be increased appropriately to improve the operating speed when designing the structure.

4 Experiment and discussion

A prototype of the proposed pipeline robot is fabricated to verify the correctness of the theoretical analysis and the numerical simulation of the dynamics model, as shown in Fig. 6. Acrylic is used to make the main body. Aluminum

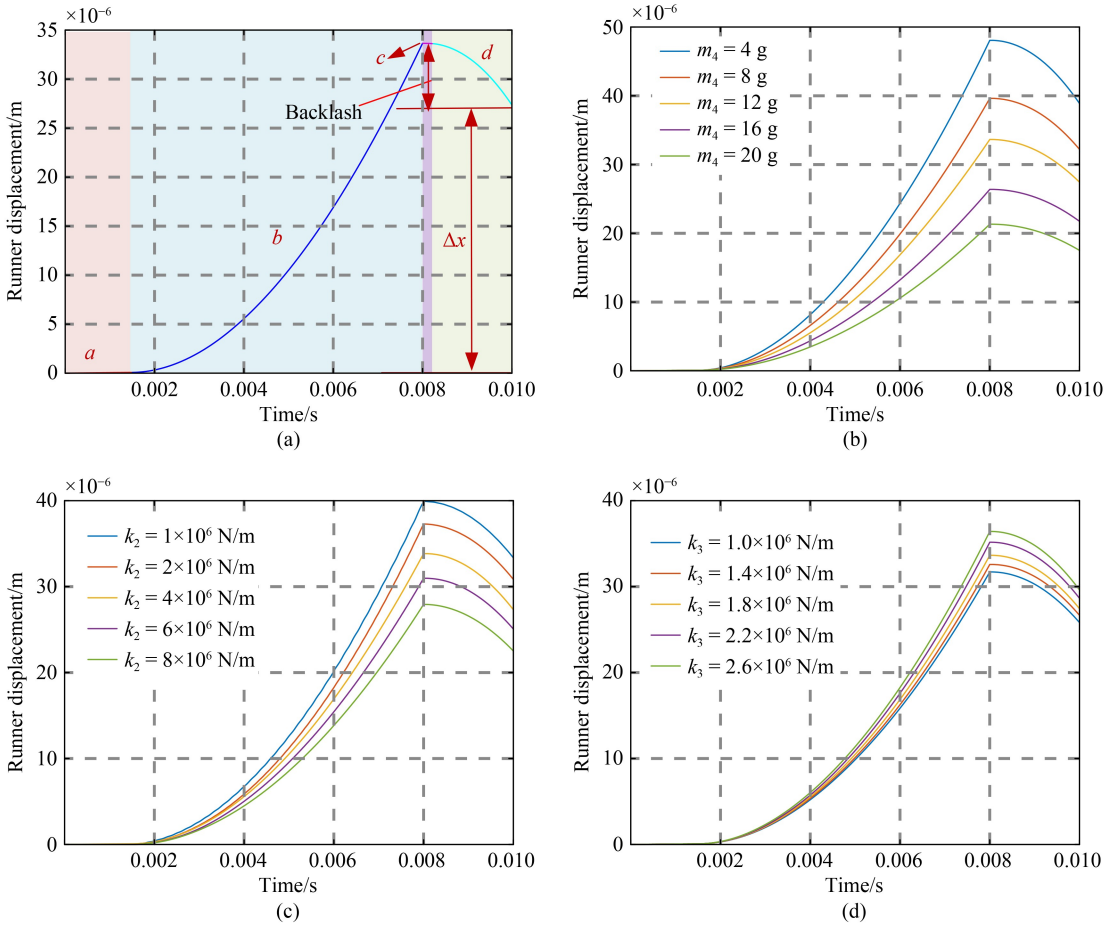

Fig. 5 Simulation for the motion trajectory of the runner: (a) motion trajectory of the runner in four phases, (b) motion trajectories of the runner with different variables m_4, (c) motion trajectories of the runner with different variables k_2, and (d) motion trajectories of the runner with different variables k_3.

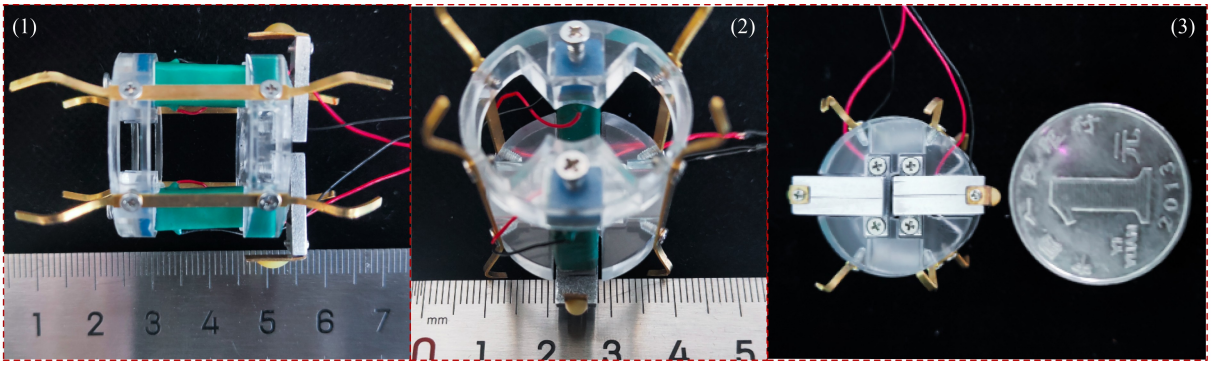

Fig. 6 Prototype of the proposed robot.

alloy 7075 is used to create the flexure hinge. The material of the support foot and drive plate spring is brass. The contact point of the driving foot is made of epoxy resin. The piezoelectric stack model is PST (20 mm × 5 mm × 5 mm). The body of the prototype has a diameter of 25 mm and a length of 30 mm. Thus, it can work in pipes with the diameter range of 25–35 mm. A test system was constructed to drive the pipeline robot and to measure the output characteristics under different drive states. The established experimental system is presented in Fig. 7. A sawtooth wave signal was generated by an arbitrary waveform generator (DG1022) and was supplied to a power amplifier (E000.B4). The power-amplified sawtooth wave signal was used to drive two piezoelectric stacks in pipeline robots. A laser Doppler vibrometer (Optomet Vector-Basis-Plus) was

applied to measure the displacement response of the proposed pipeline robot. The relationship between the output speed, displacement of the proposed pipeline robot, and the voltage, frequency, duty cycle of the excitation signal, and the external load was investigated.

4.1 Characteristics of output displacement

The sawtooth wave drive signal was set to a frequency of 100 Hz with a rising edge duty cycle of 80% for forward motion and 20% for backward motion to investigate the relationship between drive voltage and output displacement. The diameter of the test pipe was selected as 35 mm. The displacement responses of the forward and backward motions of the pipeline robot are presented in Fig. 8, which were measured by the laser Doppler vibrometer at drive signal voltages of 80, 100, and 120 V.

The observations in Fig. 8 are as follows:

1) The forward displacement response curves show a sawtooth-like waveform with the same period and drive signal, which are similar to the simulation results from the dynamics analysis, thereby verifying the correctness of the theoretical analysis. Such a form indicates that the motion of the pipeline robot will run a large step forward accompanied by a small amount of backlash in one cycle, but the overall motion direction is forward, as shown in Fig. 8(a).

2) Similarly, the pipeline robot obtains a larger inertial force on the rising edge (vertical rise) of the drive signal at a duty cycle of 20%, producing a slip phase between the driving foot and the pipe wall. A smaller inertial force on the falling edge (slow negative ramp) produces a stick phase. The entire pipeline robot moves backward, but traces of forward movement are still observed within one movement cycle, as shown in Fig. 8(b).

(3) With the increase in the peak voltage of the drive signal, the step length of the pipeline robot running in one cycle increases, and the accumulated displacement

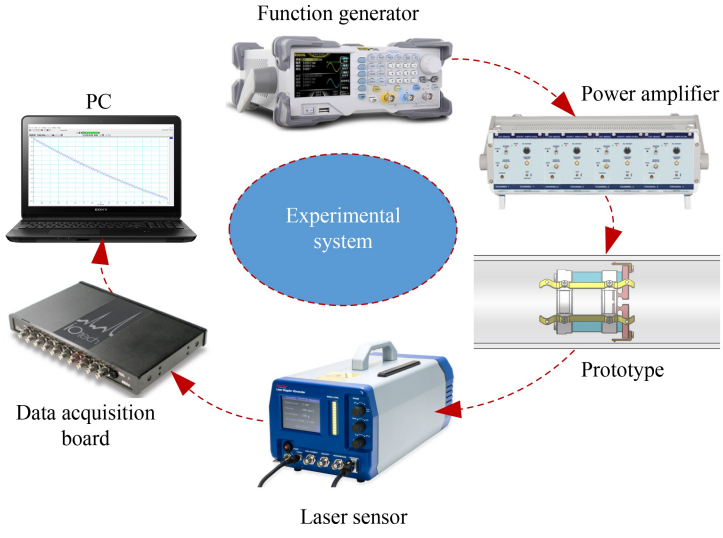

Fig. 7 Experimental system for measuring the output characteristics.

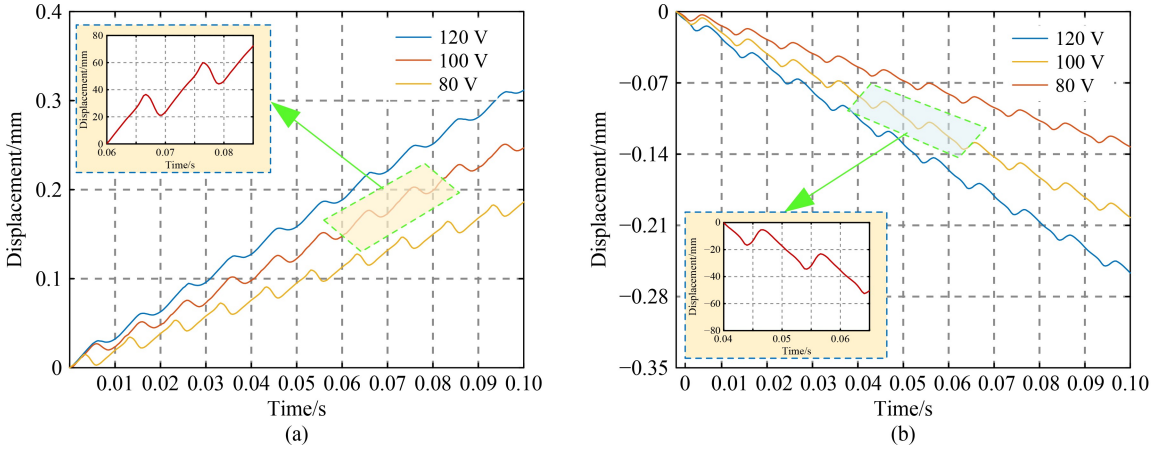

Fig. 8 Displacement response of the pipeline robot: (a) forward motion and (b) backward motion.

increases at the same drive frequency. For the forward motion, a larger drive voltage causes the driving foot to have a greater inertial force during the falling edge phase of the drive signal. The slip effect between the driving foot and pipe wall is more remarkable, and the backward displacement of the pipeline robot decreases.

A motion course of the driving foot in a cycle is taken from the test data to compare with the simulation result from Eq. (1). The test data for one step with exciting voltage peaks of 100 and 120 V, and exciting frequencies of 120 Hz are shown in Fig. 9. From Fig. 9, the two curves of the motion course are highly similar, but the values of the test data are greater than the simulation results in the whole process. At the end of the "stick" phase, the deviation between the simulation and experiment is 7 μm (6 μm) under an exciting voltage of 120 V (100 V), whereas the deviation of the whole process is 2 μm (1.5 μm). Thus, the relative deviation for a step motion is calculated to be about 6%. The reasons for the deviation are caused by larger contact stresses of the drive feet adjustment in the experiment. The deviation is also evidenced by the time of the initial "stick" phase from the two curves, that is, $t_1 < t_2$. Higher preload forces in the drive reduce the predeformation time of the bristles.

4.2 Characteristics of output speed

In the measurement of the output speed, the frequency of the drive signal frequency was set to 100 Hz, and the voltage peak of the drive signal was adjusted in the range of 20–120 V to record the speed of the pipeline robot operating forward and backward for a certain distance, as shown in Fig. 10(a). The effect of the drive frequencies on the operating speed was investigated by fixing the voltage peak of the drive signal at 120 V, as presented in Fig. 10(b). The key findings in Fig. 10 are as follows:

1) When the drive voltage amplitude is gradually adjusted from 50 to 120 V, the linearity between the robot output speed and the drive voltage amplitude is considered to be good, and the relationship between them is approximately proportional. However, Fig. 10(a) shows that a difference is observed in the speed of the forward and backward motions of the proposed robot under the same drive signal properties. The main reason for the speed difference can be explained by the fact that the friction force between the driving foot and the pipe wall is gradually decreasing during the recovery deformation of the flexure hinge and drive plate spring in the slip phase in the forward direction. The friction force between the driving foot and the pipe wall is gradually increasing during the recovery deformation of the flexure hinge and drive plate spring in the slip phase in the backward motion.

2) The output speed of the robot is positively correlated with the frequency of the drive signal. From Fig. 10(b), the output speed of the robot increases linearly with the increase in the excitation voltage frequency when the driving voltage is 120 V at the driving frequency of 50–120 Hz. The maximum output speed is 3.5 mm/s with a step distance of 30 μm for forward motion and 3 mm/s with a step distance of 25 μm for backward motion at a frequency of 120 Hz.

3) From Figs. 10(c) and 10(d), the speed of the pipeline robot is 2.98 mm/s in the forward direction, and the step distance is 30 μm when the drive voltage is 120 V. In the backward direction, the robot has a speed of 2.54 mm/s and a step distance of 25 μm. When the drive voltage is 50 V, the speed of the pipeline robot is 0.5 mm/s in the forward direction, and the step distance is 5 μm. The speed is 0.39 mm/s in the backward direction, and the step distance is 4 μm.

4) The change rate of speed difference between forward and backward motions is more obvious with the frequency and voltage of the drive signal at the lower drive frequency of 50–70 Hz and drive voltage of 50–0 V. The change rate of speed difference is insignificant at the drive signal amplitude over 70 V and drive

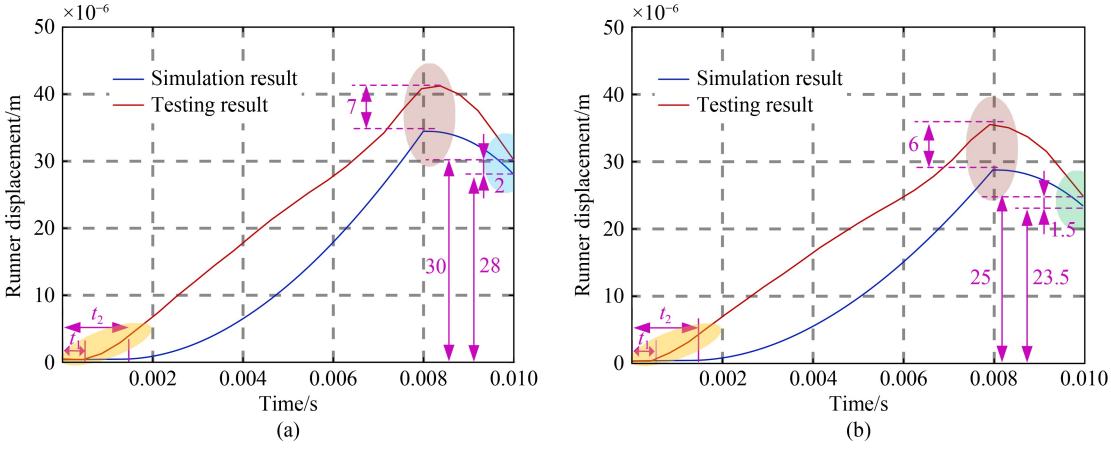

Fig. 9 Comparison of a motion course of the driving foot in a cycle: voltages of (a) 120 V and (b) 100 V.

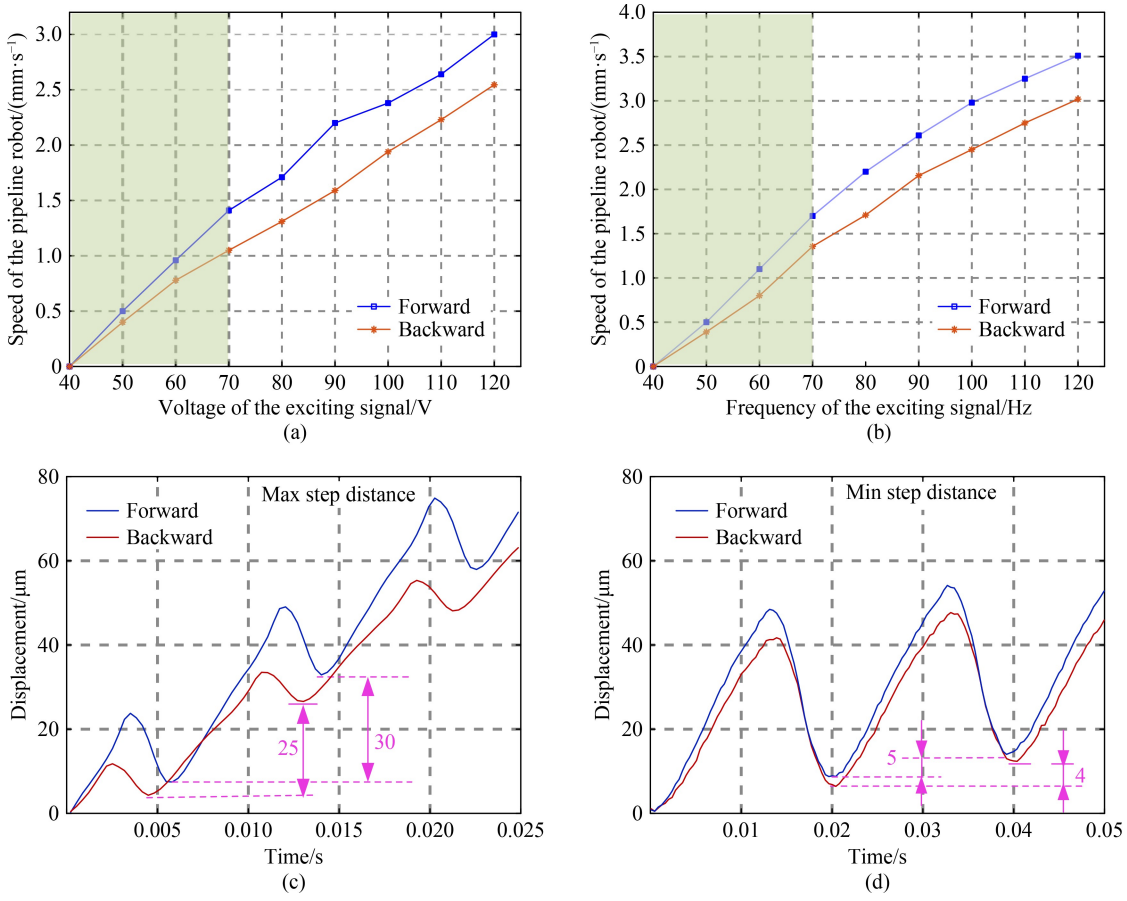

Fig. 10 Output speed of the pipeline robot under various voltages and frequencies of the drive signal: (a) changed voltages, (b) changed frequencies, (c) max step distance with drive signal of 120 V and 120 Hz, (d) min step distance with drive signal of 50 V and 50 Hz.

frequency over 70 Hz. At the lower drive frequency or lower drive voltage, the robot is in the slip phase, and the retraction is larger because the driving foot obtains a smaller inertial force. Higher stepping accuracy can be obtained in this case, but the stability of the system's operation is relatively weak from the experiment.

Theoretically, if the slope of the rising edge of the drive signal is small and the falling time is short to be infinitely close to zero, then the amount of robot backtracking will be small, and the vibration and backlash can be eliminated. However, the backlash phenomenon is inevitable in the actual drive due to the limitation of the charging and discharging times of the piezoelectric element and the mechanical response time of the system. At the same time, we can use the backlash phenomenon to improve the operating accuracy and resolution of the inertial pipeline robot. For example, if the pipeline robot moves a distance of x_1 in the stick phase, then the robot moves back a distance of x_2 in the slip phase due to the backlash. The overall displacement for a cycle time of the robot is $(x_1 - x_2)$. Therefore, a reasonable backlash will improve the resolution of the pipeline robot. On the basis of the above investigation of the effect of drive voltage and frequency on output speed, the proposed robot exhibits the maximum speed at a drive voltage of 120 V and frequency of 120 Hz. In the investigation of the effect of the drive signal duty cycle on the output speed, the drive signal was selected to have a voltage of 120 V and a frequency of 120 Hz. The speed curves of the proposed robot changed with the duty cycle of the drive voltage, as presented in Fig. 11, and the speed profile of the robot is V-shaped. When the duty cycle is 50%, the output speed of the robot is 0. If the drive signal duty cycle is greater than 50%, the robot produces a forward movement, and the speed increases linearly with the increase in the drive

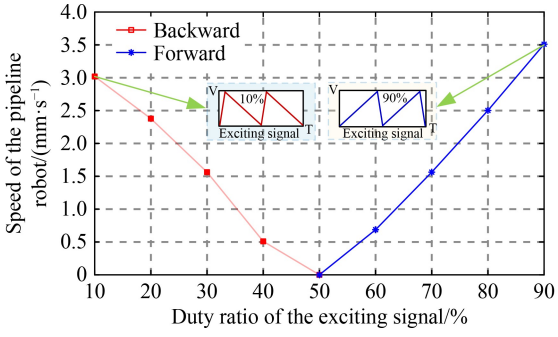

Fig. 11 Effect of drive signal duty cycle on output speed.

signal duty cycle. When the drive signal duty cycle is less than 50%, the robot moves in the reverse direction, and the speed increases linearly with the increase in the drive signal duty cycle. The robot presents a maximum speed of 3.5 mm/s in the forward direction at a duty cycle of 90% and a maximum reverse speed of 3 mm/s at a duty cycle of 10%.

4.3 Output characteristics of speed versus load

The pipeline robot was originally designed to have the ability to transport materials, carry inspection, and actuation equipment within the pipeline. Therefore, the maximum load capacity of the proposed robot needs to be investigated. Here, permanent magnets were gradually attached to the pipeline robot, and the relationship between the carrying mass of the proposed robot and the operating speed was recorded under the conditions of the drive signal voltage of 120 V, operating frequency of 120 Hz, and duty cycle of 90% for forward motion and 10% for backward motion, as shown in Fig. 12. From Fig. 12(a), the speed of the pipeline robot decreases with the increase in load. The load capacity of the robot is better when operating forward than operating backward, which is determined by the larger friction force available to the driving foot when moving forward. However, the speed of the robot is less affected by the load when the load mass is 0–20 g; when the load mass is 2040 g, the speed of the robot decreases more rapidly with the increase in load. When the load exceeds 40 g, the speed of the robot decreases with the increase in load in an approximately linear trend. When the mass of the carrying magnet is increased to 70 g (65 g), the proposed robot has no stable displacement output in forward (backward) motion. Therefore, the maximum load capacity of the robot is about 70 g for forward motion and 60 g for backward motion under the drive signal of 120 V and 120 Hz. At this point, the proposed robot carries a maximum mass of 4.6 times its own mass, where the mass of the robot is 15 g. For the climbing capacity, the proposed pipeline robot without load can climb to a pipe angle range of 0°–70°, as shown in Fig. 12(b). When the climb angle increases, the running speed of the pipeline robot drops linearly. The running speed is 0.5 mm/s with a climb angle of 70°. Figure 12(c) presents the forward motion of the pipeline robot under no load and the backward motion state when the load is 50 g at different moments. From Fig. 12(c), the speed of the pipeline robot with a load is slightly reduced compared with the unloaded state, but it still has a stable operating condition.

An acoustic levitation griper was designed to be installed into the proposed pipeline robot. The pipeline robot was endowed with the ability to transport small particles, liquid droplets, and biological tissues without contact holding. Figure 13 exhibits the process where the proposed pipeline robot carried a small particle with a diameter of 1 mm to be transported by 75 mm within 27 s. The success of this demonstration illustrates the

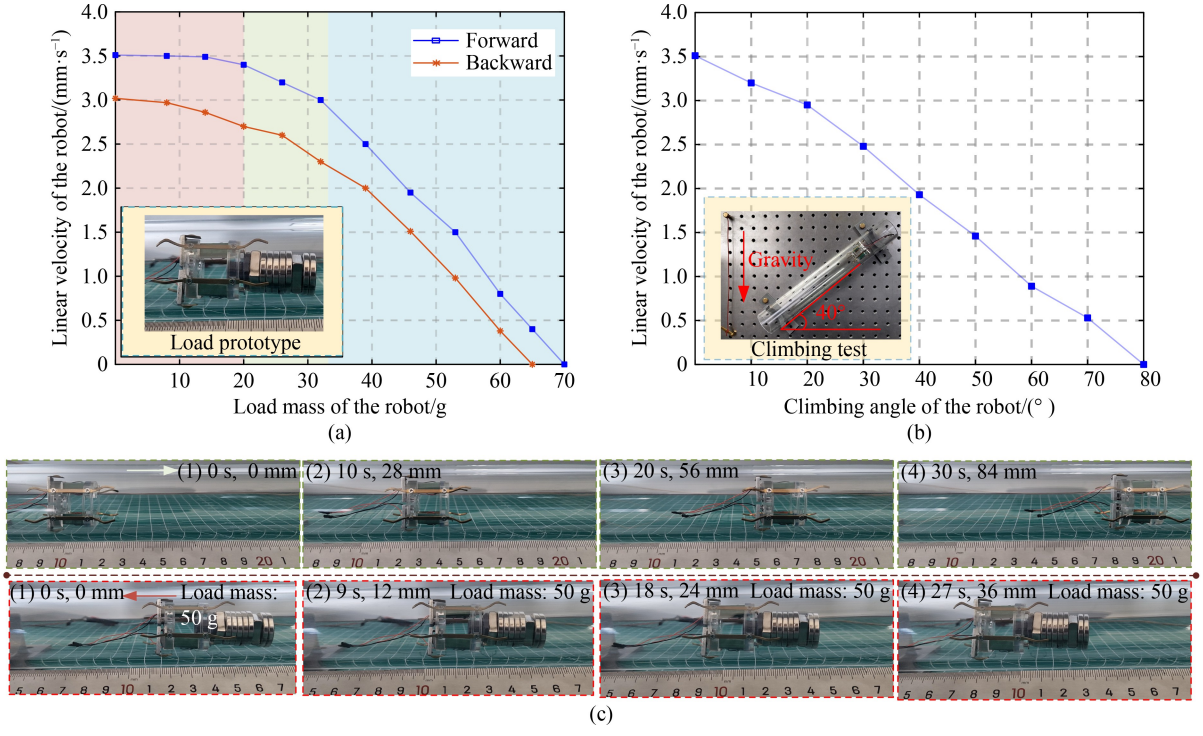

Fig. 12 Load capacity of the proposed pipeline robot: (a) relationship between load and speed, (b) climbing capacity, and (c) operating state.

potential of the proposed pipeline robot for future research in high-precision positioning and transportation in miniature pipes (e.g., test tubes) for contact-free operation. The detailed demonstration can be seen in the Electronic Supplementary Materials.

On the basis of the above experimental results, several reported typical piezoelectric inertial pipeline robots are selected for comparison to clearly show the advantages of the pipeline robot designed in this article. The results given in Table 4 [6,18,35] allow us to infer that.

1) Compared with the traditional inertial impact drive mechanism, the pipeline robot with an inertial stick-slip drive mechanism has the outstanding benefits of output performance, stepping accuracy, load capacity, and climbing ability. Some reported pipeline robots with inertial impact drive mechanisms do not have load and climbing capabilities.

2) The pipeline robot is in a moderate order of magnitude in terms of size, weight, and adaptable pipe diameter. However, if the structure is further optimized and the small size piezoelectric stacks are employed, then the size of the structure can be adapted to the pipe diameter below 20 mm, which is close to the diameter of the test tube.

3) This pipeline robot maintains a higher and stable operating speed with a slight increase in load. Although the robot employed the inertial impact drive mechanism, the variation of load can affect the matching relationship between the body mass and the inertia block, resulting in unstable output speed.

Overall, the inertial stick-slip driven pipeline robot outperforms the inertial impact driven pipeline robot in terms of accuracy and load capacity, which proves the importance and advantages of the research we have conducted.

5 Conclusions and perspectives

A small pipeline robot driven by the inertial stick-slip mechanism was proposed, and the feasibility of this drive scheme in pipeline robot applications was verified through theoretical and experimental analyses. The dynamic model of the drive system, including the LuGre friction model, was established, and the effect of the main parameters of the system on the operating state of the robot was investigated. An experimental investigation was conducted to test the relationships between output displacement, velocity, and drive signal voltage, frequency, duty cycle, and load capacity. The main conclusions of this study can be summarized as follows:

1) For the drive voltage range of 50–120 V and drive frequency of 50–120 Hz, the speed of the robot increases linearly with the increase in voltage and frequency. The maximum speed in the forward direction is 3.5 mm/s with a step of 30 μm, and the minimum speed is 0.5 mm/s with a step of 5 μm. The maximum speed in the backward direction is 3 mm/s with a step of 25 μm, and the minimum velocity is 0.39 mm/s with a step length of 4 μm.

2) The greater the rising (falling) edge duty cycle of the forward (backward) motion driven by the sawtooth wave excitation signal, the smaller the backlash of the robot motion and the greater the robot speed.

3) At a drive voltage of 120 V, a drive frequency of 120 Hz, and a duty cycle of 90%, the maximum load of the robot is 70 g, which is 4.6 times its own mass, and the maximum climb angle is 70°. This finding shows that the proposed robot has a good load capacity.

In future work, we will give the proposed pipeline robot

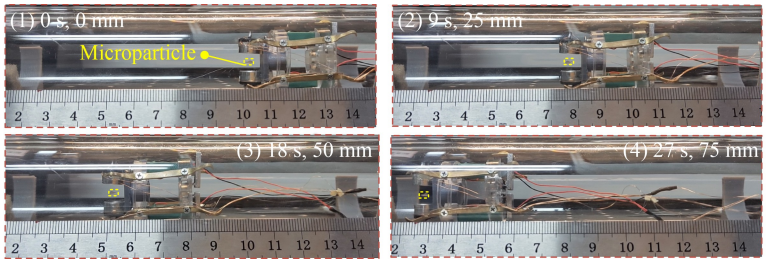

Fig. 13 Demonstration of the contactless transport of a microparticle.

Table 4 Performance comparison between the proposed pipeline robot and several typical pipeline robots [6,18,35]

Robot	Driving mode	Dimension/(mm × mm)	Weight/g	Adaptable pipe diameter/mm	Operating speed/(mm·s^{-1})		Resolution/μm	Load capacity/g	Climbing ability/(°)
					Forward	Backward			
This pipe-robot	Inertial stick-slip	30.0 × 35.0	15	20–30	3.50	3.00	4	70.0	0–70
Sun's [35]	Inertial impact	9.8 × 22.0	5	10–20	2.19	2.48	6	2.5	0–40
Takaharu's [18]	Inertial impact	10.0 × 70.0	10	10–20	5.00	–[a)]	10	–	–
Li's [6]	Inertial impact	20.0 × 55.0	30	20–30	2.86	2.69	9	–	–

Note: Parts of data are estimated with the information offered by authors. "–" indicates that the information is not available.

more diverse executive operation functions, conduct research to improve its motion stability and control accuracy, and develop its potential for biomedical applications.

Nomenclature

A	Cross section area of the piezoelectric stack
c_2, c_3	Equivalent damping of the flexure hinge and the driving foot, respectively
d_{33}	Piezoelectric coefficient
f_1	Friction between the driving foot and pipe wall
f_2	Friction between the support foot and pipe wall
F_1, F_1'	Acting force and reacting force between the driving foot and the pipe wall, respectively
F_{12}, F_{12}'	Acting force and reacting force between the piezoelectric stack and the flexure hinge, respectively
F_C	Coulomb friction force
F_p	Output force of the piezoelectric stack
F_S	Static friction force
$g(v)$	Function describing the Stribeck effect
k_1, k_2, k_3	Equivalent stiffness of the piezoelectric stack, the flexure hinge, and the driving foot, respectively
l	Length from the rotation center to the top of flexure hinge
l_1	Distance from the center of rotation of the hinge to the point of action with the piezoelectric stack
l_2	Vertical distance from the top of the flexure hinge to the center of rotation under the rotation θ_1
l_3	Vertical distance between the top of the hinge and the initial position after rotation θ_1
l_4	Length of the driving foot
L_p	Length of the piezoelectric stack
m_1, m_2, m_3, m_4	Equivalent mass of the piezoelectric stack, the flexure hinge, the driving foot, and the pipe, respectively
n	Number of the piezoelectric sheets in the piezoelectric stack
s_{33}	Elastic compliance constant of the piezoelectric stack
T	Period of the drive signal
U	Output voltage of the drive signal
v	Relative velocity of two friction surfaces
v_s	Stribeck velocity
V_{max}	Peak voltage of the drive signal
x_1	Output displacement of the piezoelectric stack
x_2, $\dot{x}_2$, $\ddot{x}_2$	Displacement, velocity, and the acceleration of the flexure hinge, respectively
x_4, $\dot{x}_4$, $\ddot{x}_4$	Displacement, velocity, and acceleration of the pipe, respectively
y_3, $\dot{y}_3$, $\ddot{y}_3$	Displacement, velocity, and acceleration of the driving foot, respectively
z	Average deformation of bristles
θ_1, θ_2	Rotation angle of flexure hinge and driving foot, respectively
Δx	Step distance of the pipeline robot and the slider
σ_0	Bristle stiffness
σ_1	Bristle damping of the bristle
σ_2	Viscous damping coefficient
μ	Friction coefficient between the driving foot and the pipe

Acknowledgements This work was supported by the State Key Laboratory of Robotics and System (HIT), China (Grant No. SKLRS-2022-KF-09). The authors declare that they have no known competing financial interests or personal relationships that could have appeared to influence the work reported in this paper.

Electronic Supplementary Materials The supplementary materials can be found in the online version of this article at https://doi.org/10.1007/s11465-022-0697-z and are accessible to authorized users.

References

1. Liu P K, Wen Z J, Sun L N. An in-pipe micro robot actuated by piezoelectric bimorphs. Chinese Science Bulletin, 2009, 54(12): 2134–2142
2. Wang L, Chen W S, Liu J K, Deng J, Liu Y X. A review of recent studies on non-resonant piezoelectric actuators. Mechanical Systems and Signal Processing, 2019, 133: 106254
3. Ciszewski M, Giergiel M, Buratowski T, Małka P. Modeling and Control of a Tracked Mobile Robot for Pipeline Inspection. Cham: Springer, 2020, 101–128
4. Guo J, Bao Z H, Fu Q, Guo S X. Design and implementation of a novel wireless modular capsule robotic system in pipe. Medical & Biological Engineering & Computing, 2020, 58(10): 2305–2324
5. Chattopadhyay P, Ghoshal S K, Majumder A, Dikshit H. Locomotion methods of pipe climbing robots: a review. Journal of Engineering Science and Technology Review, 2018, 11(4): 154–165
6. Li Z, Wang Q Z, Li J, Liu Y F, Liu C J, Cao L, Zhang W J. A new approach to classification of devices and its application to classification of in-pipe robots. In: Proceedings of 2016 IEEE the 11th Conference on Industrial Electronics and Applications. Hefei: IEEE, 2016, 1426–1431
7. Zhao C S, Zhang J T, Zhang J H, Jin J M. Development and application prospects of piezoelectric precision driving technology. Frontiers of Mechanical Engineering in China, 2008, 3(2): 119–132
8. Gargade A A, Ohol S S. Development of in-pipe inspection robot. IOSR Journal of Mechanical and Civil Engineering, 2016, 13(4): 64–72
9. Ismail I N, Anuar A, Sahari K S M, Baharuddin M Z, Fairuz M, Jalal A, Saad J M. Development of in-pipe inspection robot: a

review. In: Proceedings of 2012 IEEE Conference on Sustainable Utilization and Development in Engineering and Technology. Kuala Lumpur: IEEE, 2012, 310–315

10. Zhu X X, Wang W, Zhang S M, Liu S H. Experimental research on the frictional resistance of fluid-driven pipeline robot with small size in gas pipeline. Tribology Letters, 2017, 65(2): 49
11. Mishra D, Agrawal K K, Abbas A, Srivastava R, Yadav R S. PIG [Pipe Inspection Gauge]: an artificial dustman for cross country pipelines. Procedia Computer Science, 2019, 152: 333–340
12. Reyes-Acosta A V, Lopez-Juarez I, Osorio-Comparan R, Lefranc G. 3D pipe reconstruction employing video information from mobile robots. Applied Soft Computing, 2019, 75: 562–574
13. Qu Y, Durdevic P, Yang Z Y. Smart-spider: autonomous self-driven in-line robot for versatile pipeline inspection. IFAC-PapersOnLine, 2018, 51(8): 251–256
14. Song H, Ge K S, Qu D, Wu H P, Yang J. Design of in-pipe robot based on inertial positioning and visual detection. Advances in Mechanical Engineering, 2016, 8(9): 1687814016667679
15. Hu H, Zhang K C, Tan A H, Ruan M, Agia C, Nejat G. A sim-to-real pipeline for deep reinforcement learning for autonomous robot navigation in cluttered rough terrain. IEEE Robotics and Automation Letters, 2021, 6(4): 6569–6576
16. Kim H M, Choi Y S, Lee Y G, Choi H R. Novel mechanism for in-pipe robot based on a multiaxial differential gear mechanism. IEEE/ASME Transactions on Mechatronics, 2017, 22(1): 227–235
17. Islas-García E, Ceccarelli M, Tapia-Herrera R, Torres-SanMiguel C R. Pipeline inspection tests using a biomimetic robot. Biomimetics, 2021, 6(1): 17
18. Tokida K, Takemura K, Yokota S, Edamura K. Robotic earthworm using electro-conjugate fluid. International Journal of Applied Electromagnetics and Mechanics, 2010, 33(3–4): 1643–1651
19. Hua Y, Konyo M, Tadokoro S. Design and analysis of a pneumatic high-impact force drive mechanism for in-pipe inspection robots. Advanced Robotics, 2016, 30(19): 1260–1272
20. Nakazato Y, Sonobe Y, Toyama S. Development of in-pipe micro mobile robot using peristalsis motion driven by hydraulic pressure. In: Ananthasuresh G, Corves B, Petuya V, eds. Micromechanics and Microactuators. Mechanisms and Machine Science. Dordrecht: Springer, 2011, 23–29
21. Scharff R B N, Fang G X, Tian Y J, Wu J, Geraedts J M P, Wang C C L. Sensing and reconstruction of 3-D deformation on pneumatic soft robots. IEEE/ASME Transactions on Mechatronics, 2021, 26(4): 1877–1885
22. Yao J T, Chen X B, Chen J T, Zhang H, Li H L, Zhao Y S. Design and motion analysis of a wheel-walking bionic soft robot. Journal of Mechanical Engineering, 2019, 55(5): 27–35 (in Chinese)
23. Gao F M, Fan J C, Zhang L B, Jiang J K, He S J. Magnetic crawler climbing detection robot basing on metal magnetic memory testing technology. Robotics and Autonomous Systems, 2020, 125: 103439
24. Sattarov R R, Almaev M A. Electromagnetic worm-like locomotion system for in-pipe robots: novel design of magnetic subsystem. In: Proceedings of IOP Conference Series: Earth and Environmental Science. Krasnoyarsk: IOP Publishing, 2019, 315(6): 062013
25. Yum Y J, Hwang H, Kelemen M, Maxim V, Frankovský P. In-pipe micromachine locomotion via the inertial stepping principle. Journal of Mechanical Science and Technology, 2014, 28(8): 3237–3247
26. Kim B, Lee M G, Lee Y P, Kim Y, Lee G. An earthworm-like micro robot using shape memory alloy actuator. Sensors and Actuators A: Physical, 2006, 125(2): 429–437
27. Liu W, Jia X H, Wang F J, Jia Z Y. An in-pipe wireless swimming microrobot driven by giant magnetostrictive thin film. Sensors and Actuators A: Physical, 2010, 160(1–2): 101–108
28. Lee S K, Kim B. Design parametric study based fabrication and evaluation of in-pipe moving mechanism using shape memory alloy actuators. Journal of Mechanical Science and Technology, 2008, 22(1): 96–102
29. Deng J, Liu Y X, Zhang S J, Li J. Development of a nanopositioning platform with large travel range based on bionic quadruped piezoelectric actuator. IEEE/ASME Transactions on Mechatronics, 2021, 26(4): 2059–2070
30. Lee J, Jung W, Kim K S, Kim S. Analysis of rod vibration on a dual-slider smooth impact drive mechanism for a compact zoom lens system. In: Proceedings of 2012 IEEE/ASME International Conference on Advanced Intelligent Mechatronics. Kaohsiung: IEEE, 2012, 338–341
31. Morita T, Nishimura T, Yoshida R, Hosaka H. Resonant-type smooth impact drive mechanism actuator operating at lower input voltages. Japanese Journal of Applied Physics, 2013, 52(7S): 07HE05
32. Chen N, Zheng J J, Jiang X L, Fan S X, Fan D P. Analysis and control of micro-stepping characteristics of ultrasonic motor. Frontiers of Mechanical Engineering, 2020, 15(4): 585–599
33. Chang Q B, Liu Y X, Deng J, Zhang S J, Chen W S. Design of a precise linear-rotary positioning stage for optical focusing based on the stick-slip mechanism. Mechanical Systems and Signal Processing, 2022, 165: 108398
34. Tang J Y, Fan H Y, Liu J H, Huang H. Suppressing the backward motion of a stick–slip piezoelectric actuator by means of the sequential control method (SCM). Mechanical Systems and Signal Processing, 2020, 143: 106855
35. Idogaki T, Kanayama H, Ohya N, Suzuki H, Hattori T. Characteristics of piezoelectric locomotive mechanism for an in-pipe micro inspection machine. In: Proceedings of the Sixth International Symposium on Micro Machine and Human Science. Nagoya: IEEE, 1995, 193–195
36. Tsuruta K, Sasaya T, Shibata T, Kawahara N. Control circuit in an in-pipe wireless micro inspection robot. In: Proceedings of 2000 International Symposium on Micromechatronics and Human Science. Nagoya: IEEE, 2000, 59–64
37. Gong Z B, Luo Y, Sun L Z. Modality analysis on PZT bimorph actuator. In: Proceedings of IEEE International Conference Mechatronics and Automation. Niagara Falls: IEEE, 2005, 1863–1866
38. Sun L Z, Zhang Y N, Sun P, Gong Z B. Study on robots with PZT actuator for small pipe. In: Proceedings of 2001 International Symposium on Micromechatronics and Human Science. Nagoya: IEEE, 2001, 149–154
39. Sun L Z. Bimorph piezoelectric actuator for small pipe robot. Chinese Journal of Mechanical Engineering, 2002, 15(4): 303–307

40. Liu C L, Hu S Z, Guo H L, Wang X J, Zhang W J. Feed-forward control of stack piezoelectric actuator. Optics and Precision Engineering, 2016, 24(9): 2248–2254 (in Chinese)
41. Yang Z G, Chen X P, Cheng G M, Zeng P. Vibration analysis of in-pipe locomotive mechanism with piezoelectric bimorth. Piezoelectrics & Acoustooptics, 2000, 22(6): 410–413 (in Chinese)
42. Liu Y X, Tian X Q, Liu J K, Chen W S. China Patent, CN108540010A, 2018-09-14 (in Chinese)
43. Zhou C, Duan J A, Deng G L, Li J H. A novel high-speed jet dispenser driven by double piezoelectric stacks. IEEE Transactions on Industrial Electronics, 2017, 64(1): 412–419
44. Canudas de Wit C, Olsson H, Astrom K J, Lischinsky P. A new model for control of systems with friction. IEEE Transactions on Automatic Control, 1995, 40(3): 419–425
45. Zhong B W, Sun L N, Chen L G, Wang Z H. The dynamics study of the stick-slip driving system based on LuGre dynamic friction model. In: Proceedings of 2011 IEEE International Conference on Mechatronics and Automation. Beijing: IEEE, 2011, 584–589